Biomaterials and Biosystems 20 (2025) 100123

Contents lists available at ScienceDirect

Biomaterials and Biosystems

journal homepage: www.elsevier.com/locate/bbiosy

Development of biodegradable Fe-Mn thin structures by electroforming in deep eutectic solvents

Vinicius Sales [a], Carlo Paternoster [a], Francesco Copes [a], Paolo Mengucci [c], Gabriele Grima [d], Marcello Cabibbo [d], Georgios Kolliopoulos [b], Diego Mantovani [a,*]

[a] *Laboratory of Biomaterials and Bioengineering (LBB), CRC - I in Biomaterials and Bioengineering for Innovation in Surgery, University Hospital Research Center, Regenerative Medicine, Quebec City, G1L 3L5, Canada*

[b] *Department of Mining, Metallurgical, and Materials Engineering, Université Laval, Quebec City, G1V 0A6, Canada*

[c] *Department of Science and Engineering of Matter, Environment and Urban Planning (SIMAU), Università Politecnica delle Marche, via Brecce Bianche, I-60131 Ancona, Italy*

[d] *Department of Industrial Engineering and Mathematical Science (DIISM), Università Politecnica delle Marche, I-60131 Ancona, Italy*

ARTICLE INFO

Keywords:
Biodegradable metals
Fe-based alloys
Electroforming
Deep Eutectic Solvents
Thin structures

ABSTRACT

Fe-Mn alloys represent promising candidates for temporary biomedical intravascular implants with a thin structure (e.g., coronary, cerebral and peripheral stents) due to their high mechanical strength, acceptable biocompatibility, and controllable corrosion rate. Traditionally, these devices are produced by casting followed by thermo-mechanical processing, i.e. a time- and energy-intensive top-to-bottom approach. This study explores electroforming as an alternative method to fabricate bottom-to-top thin Fe-Mn structures using ethylene glycol-based deep eutectic solvents (DESs). Glycine was introduced as a complexing agent to enhance Mn co-deposition. Electroforming was investigated in presence of three glycine concentrations (0.2, 0.4, and 0.6 M), and the the microstructure, composition, corrosion behavior, and cytocompatibility of the developed thin (50-85 μm) structures were characterized. Higher glycine content improved Mn incorporation, crystallinity, hardness and increased corrosion rate. These findings support the use of DES-based electroforming as a promising route for fabricating biodegradable Fe-Mn devices with tunable properties.

1. Introduction

Over the years, there has been a significant increase in research focused on biomedical implants [1–4]. This surge is mainly driven by the population's desire to maintain a high quality of life. In practical clinical scenarios, such as bone healing or vessel blockages, temporary support is often the most envisaged clinical solution [5–8]. Biodegradable materials (i.e., polymers, metallic alloys, ceramics, and composites), known as bioresorbable, are rapidly become the clinical standard, allowing the diseased tissue to heal, and stepping away [9,10]. In fact, during implantation, bioresorbable implants gradually degrade [11,12].

Fe is a good candidate as a bioresorbable material [13] due to its suitable properties (i.e., mechanical properties [14], superior machinability [15] and cytocompatibility [16]). However, its low degradation rate limits its use in several clinical applications, including bone and blood contact [17–19]. Moreover, pure Fe tends to be ferromagnetic, which is limit non invasive magnetic resonance imaging (MRI) clinical follow-ups [20]. Thus, several approaches to improve the degradation rate of Fe are being explored, such as alloying with different elements (e.g., Mn) [21–24].

Fe-Mn alloys were introduced for biomedical devices such as coronary stents [25]. Mn is essential in several body functions, specifically bone formation, calcium absorption, blood sugar regulation, and fat and carbohydrate metabolism [26]. Moreover, Mn standard electrode potential is more negative (– 1.18 V) than Fe (– 0.44 V), so when Fe and Mn form a solid solution, the standard electrode potential is shifted to more negative values, increasing its degradation rate [13]. Recent studies were performed to improve Fe-Mn alloy properties. Xu et al. [16] reported that the as-cast Fe-30Mn-1C alloy significantly improved UTS and elongation up to 1010 MPa and 88 %, respectively. Those values exceeded 316 L SS (490 MPa, 40 %). An enhanced degradation behavior was observed for Fe-30Mn-6Si and Fe-30Mn-1C alloys compared to Fe-30Mn alloys [27].

In the past decade, electroforming has been studied as an alternative

---

* Corresponding author at: Dept Min-Met-Materials Eng, Director, Laboratory for Biomaterials and Bioengineering, Laval University, Quebec City, Canada.
E-mail address: diego.mantovani@gmn.ulaval.ca (D. Mantovani).

https://doi.org/10.1016/j.bbiosy.2025.100123
Received 30 July 2025; Received in revised form 12 September 2025; Accepted 16 September 2025

method to fabricate thin metallic structures for implants (i.e., stents) [28]. Electroforming is an electrodeposition process similar to electroplating and electrorefining. After the end of the deposition cycle, the deposited metal is later separated from the substrate or mandrel [29]. This process has proven successful for fabricating thin-walled structures due to its ability to build materials bottom-to-top layer-by-layer [30]. Electroforming is limited to metals that can be electroplated, which restricts the choice if an aqueous electrolyte solution is used; In this case, elements like Ni [31], Cu [32], and certain precious metals [33] can be easily deposited. This limitation is related to the hydrogen evolution reaction [34] due to the preferential reduction of water when metals with negative reduction potential (i.e., Mn) are electrodeposited. Deep Eutectic Solvents (DESs) have been considered to overcome these drawbacks.

DESs are a non-aqueous electrolyte generally composed of a metal salt and a hydrogen bond donor (i.e., Ethylene Glycol) [35–37]. In recent years, DESs have been applied to electrodeposition of functional alloys, enabling control of structure and properties for diverse applications. Cu-Ag nanostructures with tunable morphology have been prepared in ChCl-urea DESs for catalytic and electronic uses [38], while Fe-Co-Ni alloys obtained in ChCl-based DESs improved magnetic properties [39,40]. DESs have also enabled the electrodeposition of reactive metals such as Mg for lightweight structural applications [41], and systematic studies on Fe-Cr alloys demonstrated that electrolyte composition governs the formation of dense coatings for protective purposes [42]. Additives have also been applied to improve the electrodeposition process when combined with DESs. The presence of additives has been shown to influence the physical and mechanical properties of the deposits, such as grain size, brightness, internal stress, and chemical composition [43]. They influence the growth and crystallinity of the resulting deposits [44]. Previous studies have shown that additives can function as either catalysts or inhibitors during electrodeposition. This behavior occurs through their ability to promote complex formation between metal ions and increase individual ions' activation polarization by blocking active sites on the substrate [45,46]. They can be chosen according to the required final properties of the electrodeposited metals or alloys. Alesary et al. [45] studied the effect of nicotinic acid, boric acid, and benzoquinone as additives in ChCl/Ethylene glycol-based DES for electrodepositing zinc. They noticed that the studied additives decreased the current efficiency of the process from 95 % (without additives) to 52 % using nicotinic acid. Guo et al. [47] investigate the effect of glycine as an additive in ChCl/urea-based DES to electrodeposit Ni-Mn alloys. Increasing the amount of glycine in the electrolyte improved the co-deposition of Mn in the Ni matrix.

This work aims to co-deposit Fe and Mn using a deep eutectic solvent (DES) based on ethylene glycol, Fe, and Mn chloride salts. This study hypothesizes that adding glycine as a complexing agent will enhance Mn incorporation during electroforming, thereby tuning the alloy microstructure and crystallinity. Fe-Mn foils were electroformed with different glycine concentrations (0.2, 0.4, and 0.6 M), and their structural, electrochemical, mechanical, and biological properties were systematically evaluated. The objective was to establish processing–structure–property relationships that may guide the design of bioresorbable Fe-Mn alloys for potential biomedical applications.

2. Experimental

2.1. Materials

Ethylene glycol (acronym: EG, anhydrous, 99.8 %, Sigma Aldrich), glycine (Sigma Aldrich), $FeCl_2•4H_2O$ (Ward's Science), $MnCl_2$ (99 %, Acros Organics). H_3BO_3 (Fisher Scientific) and $CaCl_2$ (Fisher Scientific) were added to the electrolyte. These additives act as a cathodic polarization agent [48] and an internal stress reducer [28] respectively. The chemical composition of the electrolytes is presented in the supplementary information (Table SI 1). Each electrolyte was produced by mixing and stirring all chemicals at 80 °C using a hot plate until a homogeneous solution was obtained (around 30 min). Three concentrations of glycine (0.2, 0.4, and 0.6 M) were selected based on literature reports [47,49] showing that low levels of glycine (0.1 – 0.2 M) influence Mn incorporation in DES-based systems. Extending this range allowed to evaluate whether higher concentrations could further modulate Mn content, crystallinity, and degradation kinetics, as well as to identify a processing window that ensures deposition stability.

2.2. Electrolyte characterization

An Agilent Cary 660 ATR-FTIR (Agilent Technologies, USA) device was used to analyze the chemical bonds of the electrolytes. The system featured a detector and beam splitter composed of deuterated l-alanine doped triglycine sulfate (DLa-TGS) and a Ge-coated KBr crystal. Measurements were taken within the wavenumber range of 4000 to 400 cm^{-1}. The spectra were recorded under atmospheric pressure at a temperature $T = 25 \pm 1$ °C.

Cyclic voltammetry (CV) test was performed using a three-electrode cell and 100 mL capacity. The cell was connected to a Potentiostat/Galvanostat Versastat 3. A titanium foil (1.0 cm^2) welded with a conductive wire (connexion) and embedded in epoxy resin was used as a working electrode (WE), a graphite rod (2.0 cm^2) as a counter electrode (CE), and a silver wire (0.5 cm^2) as a reference electrode (RE). The titanium surface was previously polished with sandpaper until 1200-grit. The electrolyte temperature was kept stable at 80 °C using a heating plate. The CV test allows the investigation of the effect of glycine concentration on the cathodic and anodic current and the reduction and oxidation potentials. A range of +2.0 V to –2.0 V and a scan rate of 20mV/s were investigated.

2.3. Electroforming

Electroforming was performed on Ti working electrodes with an exposed surface area of 1×1 cm^2 and the same electrochemical setup used in CV tests. After deposition, the foils were detached by mechanical peeling using a sharp blade edge. The tests were performed by applying a current density of 30 mA/cm^2 for 3 h. After the electrodeposition, the electroformed material was mechanically stripped off the titanium surface using a sharp blade edge, cleaned with isopropanol (99.9 %), and dried with compressed air. A scheme of the electrochemical workstation used in this study is presented in the supplementary information (Fig. SI 1). Also, the samples were weighted, and the current efficiency was calculated using the ratio between the measured mass and the theoretical weight obtained by Faraday's law.

2.4. Microstructure, roughness, and chemical characterization

The specimens, both for optical and electron microscopy and microanalysis, were prepared by mounting them in epoxy resin in a vertical way, polishing with silicon carbide (SiC) paper up to 1200 grit, and performing a final polishing using a 0.05 μm alumina emulsion. After polishing, the samples were chemically etched using Nital 1 %, and their cross-sections were analyzed using an optical microscope Nikon Epiphot. A scanning electron microscope (SEM, FEI QUANTA 250) operating at 15 kV was utilized to examine the surface morphology of the electroformed alloys. An energy-dispersive X-ray (EDX) analysis was conducted to determine the alloy composition. The chemical distribution of Fe, Mn, and O and their respective concentration across the thickness of the samples was evaluated using electron probe microanalysis (EPMA, Cameca SX-10) mapping with a 20 nA probe current and 15 kV accelerating voltage, and acquisition spots spaced ~3 μm apart. The surface roughness was obtained by a profilometer (DektakXT, Bruker, Germany). The map scan was assessed using the software Vision 64 (Bruker); a length of 1000 μm, a radius of 12.5 μm, a resolution of 0.6

μm/point, and a stylus force of 1 mg were investigated.

2.5. *Corrosion behavior*

The corrosion tests were conducted using the same potentiostat platform used for the electroforming process, with the samples analyzed in their as-produced state. These tests were performed in three samples per condition using Hank's buffered saline solution (HBSS, Thermofisher product number 14,175,095) from Gibco, which simulates the ionic composition of blood plasma. The formulation of this solution is detailed in the supplementary information Table SI 2.

Corrosion tests were conducted using a three-electrode mini-cell system (MCS) (Ibendorf & Co. GmbH, Bernau bei Berlin, Germany) [23, 24]. The MCS consisted of a plastic tip, a tube containing a saturated calomel electrode (SCE) as the reference electrode, and a platinum counter-electrode. The working electrode was the sample surface in contact with the plastic tip. The electrical contact was established using a conductive copper adhesive stripe on the sample's backside and a clamp to ensure good conductivity between the components. The MCS was filled with 3 mL of HBSS. The electrochemical tests began with determining the open circuit potential (OCP), which was recorded for 1 hour. Following OCP measurements, electrochemical impedance spectroscopy (EIS) was carried out. A frequency range from 100 kHz to 10 mHz at a potential amplitude of ± 10 mV vs. OCP was investigated. Potentiodynamic polarization tests (PDP) were also conducted, analyzing a potential range from – 0.2 V vs. OCP to + 1.0 V vs. OCP at a scan rate of 0.166 mV/s. The corrosion rate (CR) was determined by the Tafel extrapolation of the PDP curves to obtain i_{corr} and applying in Eq. (1) based on ASTM G102–23 [50] standard:

$$\boldsymbol{CR} = \boldsymbol{K}_1 \frac{\boldsymbol{i_{corr}}\ .\boldsymbol{EW}}{\boldsymbol{\rho}\ .\boldsymbol{A}} \tag{1}$$

Where CR refers to the corrosion rate (mm/yr), $K_1 = 3.27 \times 10^{-3}$ mm μA^{-1} cm^{-1} yr^{-1}, i_{corr} represents the corrosion current (A), A is the exposed surface area (cm^2), ρ stands for the density of the metal (g/cm^3), EW refers to the equivalent weight (g).

$$EW = \frac{1}{\sum \frac{n_i f_i}{W_i}} \tag{2}$$

Where n_i is the valence of the i^{th} element of the alloy, f_i is the mass fraction of the i^{th} element of the alloy, and W_i refers to the atomic weight of the i^{th} element in the alloy.

2.6. *Mechanical properties*

Following the completion of the manufacturing process, samples were embedded perpendicularly to the built direction to facilitate observation of the deposited layers' morphology and characteristics. Cross-section specimens were mounted in acrylic resin (Struers), polished with 1000/4000 grit SiC paper, and subsequently polished with an oily suspension of synthetic diamond paste (25 nm diameter). Micrographs were obtained using a Leica DVM6 digital microscope, with a maximum field of view of 3.60 mm. In particular, the microscope was used with a magnification of 50x, equivalent to that of a classical inverted optical microscope lens, to scan the surfaces of the samples to identify any irregularities and examine the deposition patterns obtained through the electroforming technique. The scanning process revealed the existence of several fundamental regions, the locations of which were mapped for subsequent analysis of their mechanical performance via microhardness testing. In particular, microhardness tests were conducted on the polished cross-section using a Qness 60A EVO machine with loads of 25 gF and 50 gF, respectively. Two different indenter types were employed: the Vickers indenter was used following the ISO 6507 to facilitate comparison with existing data from the literature. The Knopp indenter was selected for its suitability for analyzing thin layers and hard materials. Before conducting the microhardness test on thin layers, a calibration test was performed on a Hadfield steel plate sample to obtain the load-hardness curve. Subsequently, electroformed specimens were tested, wherein differentiated test patterns were created based on the deposited morphology and element segregation mapped during optical microscope observation. Samples exhibiting homogeneous element distribution were analyzed with a single line of five prints for Vickers and Knopp at 25 gF and 50 gF. Conversely, samples exhibiting element segregation in layered stripes underwent testing utilizing five test values for each indenter and load on two lines differing in their configuration based on the disparate methods of elemental mixing observed during the electrodeposition process. The lower and upper regions of the built plate are typically the areas of interest. Following ISO 4545, the dwell time for each test was set to ten seconds.

2.7. *Crystallography*

The crystallographic structure of the electroformed samples was characterized using X-ray Diffractometry (Siemens® D5000) with Cu-Kα radiation (λ = 1.5406 Å, 40 kV), a step size of 0.02°, and a graphite monochromator (TX, USA). Peak identification was performed using DIFFRAC.EVA software (Bruker AXS, 2008), and attributed with the PDF database from the International Centre for Diffraction Data (ICDD).

2.8. *Biological tests*

Before starting the tests, all samples were sterilized with UV irradiation. Briefly, each side of the samples underwent two 15-minute cycles of UV irradiation. After that, samples were stored in a sterile 24 multi-well plate until use.

2.8.1. *Cell culture*

Human umbilical vein endothelial cells (HUVECs) were used in this study. Cells were isolated from human umbilical cord samples obtained from normal-term pregnancies. All experiments were performed in compliance with the Canadian Tri-Council Policy Statement: Ethical Conduct for Research Involving Humans and institutional CHU de Quebec - Laval University guidelines. The protocol was approved by the Ethics Committee of the CHU de Quebec Research Centre (CER #S11–03–168). The cells were seeded in M199 culture medium (Gibco, Invitrogen Corporation, Burlington, ON, Canada) with 5 % fetal bovine serum (FBS, Gibco, Invitrogen Corporation, Burlington, ON, Canada), 1 % P/S (Gibco, Invitrogen Corporation, Burlington, ON, Canada), 2 ng/ml fibroblast growth factor (FGF, Life Sciences, Grand Island, NY, USA), 1 ng/ml endothelial growth factor (EGF, Life Sciences, Grand Island, NY, USA), 1 μg/ml ascorbic acid (Sigma Aldrich, Oakville, ON, Canada), 1 μg/ml hydrocortisone (Sigma Aldrich, Oakville, ON, Canada) in a 75 cm^2 flask and then maintained in culture at 37 °C in a saturated atmosphere at 5 % CO_2. The culture medium was changed every 48 h. When 85 % - 90 % of confluence was reached, cells were then enzymatically detached from the plate (0.05 % trypsin, Gibco, Invitrogen Corporation, Burlington, ON, Canada) and then reseeded at a ratio of 1:3 or used for experiments. The cells have been used in passages 4 and 5 for the reported experiment.

2.8.2. *Indirect viability assay*

The indirect cytotoxicity test was performed following the ISO 10,993–5:2009 procedure. Briefly, the samples were immersed in 440 μl of M199 culture medium, supplemented with 1 % penicillin-streptomycin for 1, 3, and 7 days. At each time, the medium was collected from the samples and subsequently used for the viability test. Viability tests have been performed using different extracted media concentrations: 100 %, 10 %, and 1 %. Before putting them in contact with cells, extracted media were supplemented with 10 % fetal bovine serum (FBS), 2 ng/mL recombinant Human Fibroblast Growth Factor–basic (FGF), 0.5 ng/mL recombinant Human Epidermal Growth

Factor (EGF), 1 µg/mL ascorbic acid, 1 µg/mL hydrocortisone and 90 µg/mL heparin (Sigma). For the 10 % and 1 % dilutions, extracted media were diluted with complete M199 medium (M199 medium supplemented with the reagents mentioned above). One day before contact with the extract, HUVECs were seeded in the well of a 96 multi-well plate at a density of 20,000 cells/cm^2 and incubated at 37 °C and 5 vol. % CO_2 for 24 h in 100 µl/well of complete M199. The day after, the medium was removed, and 100 µl of the 100, 10, and 1 % extract concentrations were added to the well containing the HUVEC and incubated for 24 hrs. Normal culture medium was used as a control (CTRL). The extracts concentrations and control medium were then removed, and 100 µL of 1 % solution of resazurin sodium salt in complete M199 medium was added to the cells and incubated for 4 h at 37 °C and 5 vol. % CO_2. After the incubation, the solutions containing the now reduced resorufin product were collected, and fluorescence intensity at a 545 nm$_{ex}$/590 nm$_{em}$ wavelength was measured with a SpectraMax i3x Multi-Mode Plate Reader). Fluorescence intensity is proportional to cell viability.

2.8.3. *Statistical analysis*

Statistical significance has been calculated using ANOVA non-parametric Kruskal-Wallis method with Dunn post-test through the software InStat ™. Values of $p < 0.05$ or less have been considered significant.

3. Results

3.1. *Electrolyte cyclic voltammetry*

Before the electroforming process, cyclic voltammetry tests of the electrolytes were performed. The obtained curves can be observed in Fig. 1a. The analysis was carried out between –2.0 V and + 1.6 V. In the voltage interval of 0 V and – 0.2 V, it was possible to observe the formation of a small cathodic peak (negative current density) attributed to reducing some Fe^{3+} species to Fe^{2+}. From the potential of – 0.8 V to – 2.0 V, a second cathodic peak was observed due mainly to the second reduction of Fe^{2+} to metallic iron Fe^0 [51,52]. Close to – 2.0 V, the reduction of Mn^{2+} to metallic manganese Mn^0 was reported [53]. It was observed that increasing glycine concentration showed a decrease in the reduction current at the second reduction peak. This decrease can be related to the formation of a complex compound between glycine and Fe^{2+}, which finally inhibits the reduction of Fe^{2+}[47]. The competition for active sites on the surface of the electrode is usually seen during electrodeposition with organic additives, either by the organic molecule itself or by a metal cation species complexed with the organic molecule. Such adsorbed species can completely cover the surface, and the inhibition effect saturates at a very low concentration [49]. Similar findings were observed by Guo et al. [47] in their study of electrodeposition of Ni-Mn [53]. The same behavior was noticed in the oxidation curve (positive current density) between – 0.8 V and + 1.2 V, representing the oxidation of Fe^0 to $Fe^{2+}$and Mn^0 to Mn^{2+}. Fig. 1b shows the deposition potential curves during 3 h of electrodeposition. It was observed that the addition of glycine shifted the potential to negative or cathodic values, allowing the reduction of Mn^{2+} to metallic Mn^0 [54].

3.2. *Surface morphology and chemical composition*

The electroformed samples and their respective SEM micrographs can be observed in Fig. 2. It was noticed that the concentration of glycine affected the morphology of the obtained alloys. The condition G00 (Fig. 2a) showed a microstructure with well-developed surface cubic features [52]. Condition G02 (Fig. 2b) produced a surface with a cubic shape again; however, the size of the cubes decreased on average compared to condition G00. Increasing the amount of glycine to higher concentrations, like in conditions G04 (Fig. 2c) and G06 (Fig. 2d) showed a structure with a diminution of the cubic shape particles and an increase of a general needle-shaped, becoming finer and finer. A more negative deposition potential may lead to supersaturation at the interface, resulting in a needle-shaped growth [55]. Condition G06 showed the formation of round-shaped clusters of different sizes. This morphology was well observed at high magnification (1000 ×) and could be related to the Fe-Mn co-deposition competing with Fe in the nucleation site [56]. The current efficiency of the process for the conditions (G02, G04, and G06) increased compared to G00, respectively, from 75 % to ~88 %. The cross-section morphology changed within the glycine concentration [66]. G02, G04, and G06 showed needle-shaped growth [48]. The chemical etching revealed a layer-by-layer microstructure for G04. The same feature was noticed in conditions G02 and G06. On a stepwise surface, the atoms attach to kinks at the steps, resulting in the motion of steps along the plane until the whole layer is covered. This mechanism is called a layer-by-layer growth mode [57]. Condition G06 showed signs of chemical etching at the lower layer (surface in contact with the substrate), as seen in Fig. 2d Based on the EPMA analysis, it was observed a predominant presence of Fe. Condition G00 presented a lower amount of oxygen, indicating a low oxidation on its surface. The conditions containing glycine (G02, G04, and G06) demonstrated a significant oxygen increase and favored Mn's appearance, indicating the incorporation of Mn into the electroformed samples.

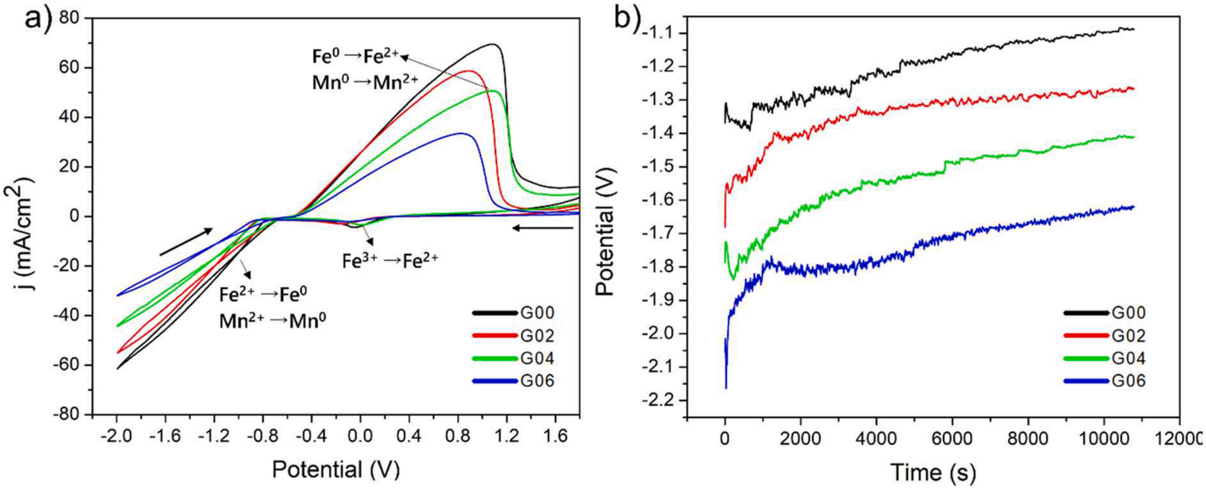

Fig. 1. a) Cyclic voltammograms of the electrolytes without (G00) and with different concentrations of glycine (G02, G04, and G06) at $T = 80$ °C, obtained with a scan rate of 20 mV/s. b) Chronopotentiometry curves obtained during 3 h of the electroforming process.

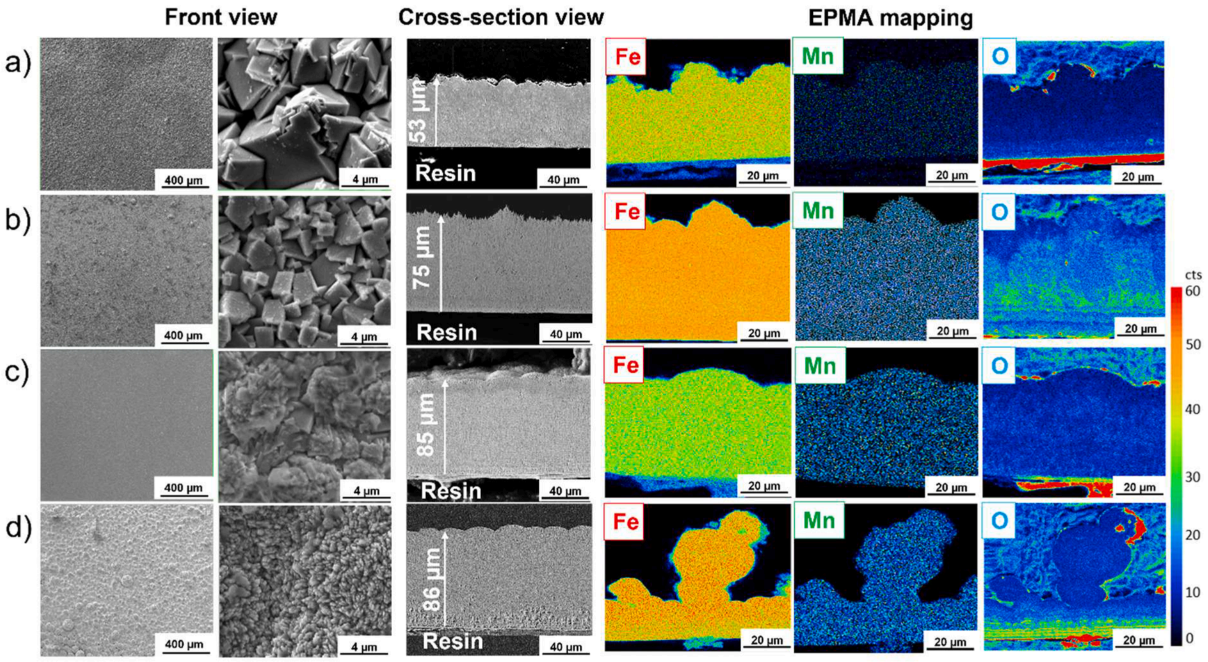

Fig. 2. Electroformed samples and respective scanning electron micrography at different magnifications (100 ×, 1000 ×, and 10,000 ×) of front and cross-section views with respective EPMA mapping distribution of elements Fe, Mn, and O. They were produced using EG-based electrolytes without glycine a) G00 and with glycine b) G02, c) G04, and d) G06 at 80 °C for 3 h.

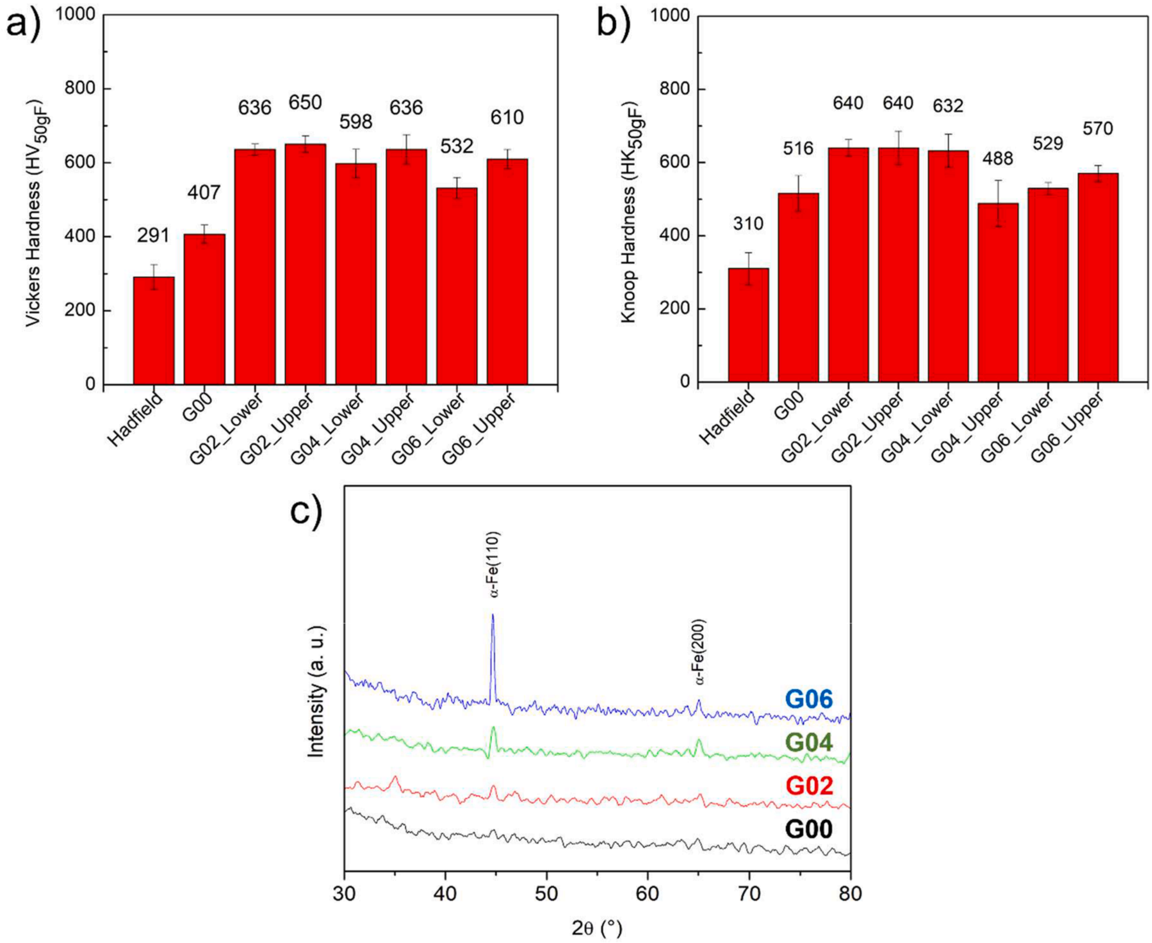

Fig. 3. a) Vickers and (b) Knoop hardness of Hadfield steel and samples obtained in the EG-based DES. For glycine-containing conditions (G02, G04, G06), hardness was measured separately in the upper and lower layers. c) XRD patterns of samples produced without glycine (G00) and with glycine additions (G02, G04, G06).

Condition G06 showed a different cross-section chemical distribution with lower layers in O and Mn than the upper layer (contact with electrolyte), indicating a preferential Mn-rich degradation zone (Figure SI 7).

3.3. Mechanical properties and cristallography

The measured Vickers and Knoop hardness of the electroformed samples produced without and with glycine are presented in Fig. 3. It was possible to observe that the electroformed samples presented a higher hardness than a commercial Hadfield alloy. Also, adding glycine to the electrolyte significantly increased the material's hardness in both Vickers (from 407 HV to ~600 HV) and Knoop (from 516 HK to ~630 HK) analysis. Comparing the hardness in upper and lower layers, condition G06 presented a significant variation when measured using the Vickers technique (Fig. 3a), presenting 532 HV in lower layers and 610 HV in upper layers. Condition G04, tested using Knoop (Fig. 3b), showed the most significant variation, indicating the formation of less hard layers close to the surface. Comparing the conditions containing glycine, the lower layers of condition G06 presented the lowest hardness values (532 HV and 529 HK). Complementary data and statistical analysis are provided in the supplementary information.

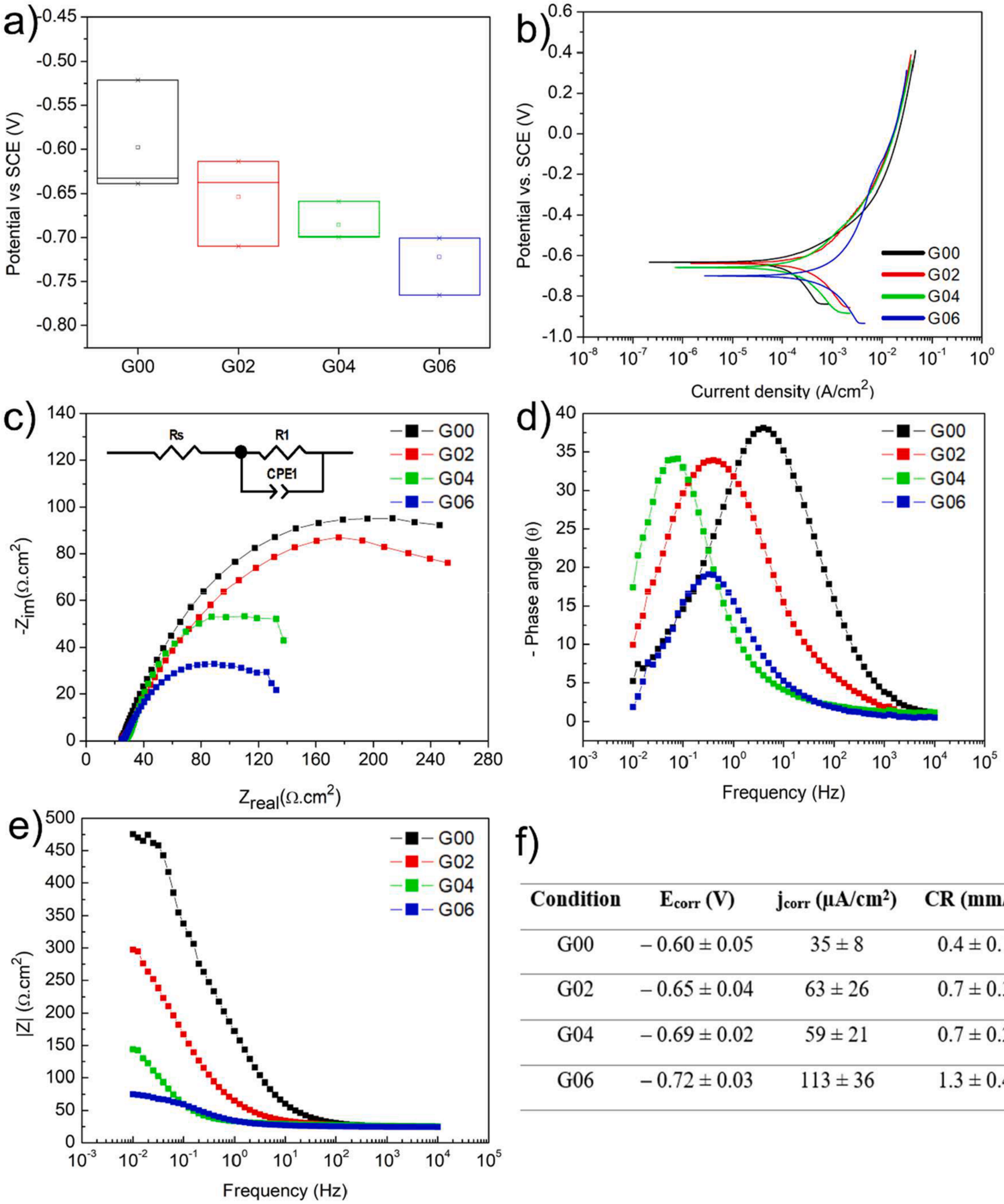

Condition	E_{corr} (V)	j_{corr} ($\mu A/cm^2$)	CR (mm/y)
G00	− 0.60 ± 0.05	35 ± 8	0.4 ± 0.1
G02	− 0.65 ± 0.04	63 ± 26	0.7 ± 0.3
G04	− 0.69 ± 0.02	59 ± 21	0.7 ± 0.2
G06	− 0.72 ± 0.03	113 ± 36	1.3 ± 0.4

Fig. 4. a) Average corrosion potential measured after 1 hour of OCP using HBSS solution carbon counter electrode and saturated calomel (SCE) reference electrode; b) Polarization curves of electroformed Fe (G00) and Fe-Mn alloys (0.2 M, 0.4 M, and 0.6 M of glycine) obtained with a scan rate of 0.166 mV/s, Electrochemical impedance spectroscopy obtained after 1 hour OCP measurements c) Nyquist and electrical equivalent circuit; d) Bode modulus; e) Bode phase; and f) Corrosion potential E_{corr} (V), corrosion current density j_{corr} ($\mu A/cm^2$), and corrosion rate CR (mm/year) in Hank's solution.

The XRD spectra of the electroformed samples are shown in Fig. 3c. It was possible to observe that the addition of glycine influenced the crystallization of the electroformed samples. The conditions G04 and G06 presented a characteristic pattern of crystalline αFe with bcc structure (JCPDS 06 – 0696) [28] as indicated by the peaks (110) and (200) [15,52]. The conditions without (G00) and a low amount of glycine (G02) presented a decrease in the peak's intensity, indicating a poor crystallization or an amorphous structure. Similar finds were observed by Guo et al. [47]. They studied the effect of glycine addition in Ni-Mn deposition using ChCl/Urea DES in 4 different current densities (1, 3, 6, and 9 mA/cm^2). They noticed that increasing the current density, the crystallographic intensity decreased. This behavior could be related to a fast nucleation process [53].

3.4. Corrosion

The electrochemical properties and the corrosion resistance of the electroformed samples were investigated. Fig. 4a shows the corrosion potential (E_{corr}) obtained after the OCP. The electroformed alloys' potential shifted to more cathodic or less noble potential values within increasing glycine concentration. The polarization curves are presented in Fig. 4b It was possible to observe that the condition G06 had an increase (113 μA/cm^2) in the corrosion current density (j_{corr}) compared to G00 (35 μA/cm^2). Consequently, the corrosion rate increased from 0.4 mm/yr to 1.3 mm/yr. The values of E_{corr}, $j_{corr,}$ and corrosion rate can be seen in Fig. 4f.

EIS was applied to characterize the corrosion processes at the interface metal surface/electrolyte (i.e., ion diffusion, double-layer charging, and oxide formation) [58]. The impedance values are presented through the Nyquist diagrams (Fig. 4c). Only one semi-circle was observed in each studied condition. Condition G00 presented the highest impedance values, indicating a higher corrosion resistance [59,60]. The high glycine-containing conditions (G04 and G06) presented the lowest impedance values. These could be related to their highest content of Mn. Fig. 4d shows the plot of Bode as a function of the phase angle. Analyzing the plots, a capacitive peak formed at medium frequencies (~10^1 Hz) for the condition G00. This condition presented the highest phase angle value, indicating a higher corrosion resistance [61]. Conditions G02, G04, and G06 also showed one capacitive peak at lower frequencies (~10^1 – 10^{-2} Hz) due to an active degradation process. Fig. 4e shows the impedance modulus Bode plot. The curves showed three parts, the first at high frequencies (~10^2–10^4) representing the resistance of the electrolyte. In the frequency range from ~10° to ~10^{-1}, it was possible to observe an increase in the impedance. This behavior was associated with the double layer's resistance in the interface metal-electrolyte. The last region at low frequencies (~10^{-2}) represented the metal charge transfer resistance. The curves of EIS were fitted, and an electric equivalent circuit (EEC) was obtained Fig. 4f. The circuit was similar for all the studied conditions, and it was composed of an electrolyte resistance (Rs) connected in series with a parallel combination of a resistor (R1) representing the double layer or charge transfer resistance and a constant phase element (CPE1) representing the capacitance of the double layer. CPE represented a non-ideal electrical capacitor, and it was related to material attributes like surface heterogeneities and roughness [62,63] It was characterized by the exponent "n", which is an empirical parameter ($0 < n < 1$) correlated to the shift of the phase angle. If $n = 1$, CPE represents a pure capacitor; if $n = 0.5$, it is associated with a Warburg impedance and, for $n = 0$, a pure resistance [64]. In this work, the values of n were higher than 0.6, indicating mainly a capacitive behavior of the sample surface. The fitted data for Rs, R1, CPE1, and n are presented in the supplementary information (Table SI 5).

3.5. Cell viability

Alamar Blue assays were performed on HUVECs exposed to extracts at 100 %, 10 %, and 1 % concentrations to assess the effect of degradation products on cell viability. At 100 % extract, all conditions completely suppressed metabolic activity at all time points, indicating the absence of viable cells. At 10 %, viability partially recovered but remained significantly lower than CTRL, with no differences among groups; complete data for these two dilutions are provided in the Supplementary Information (Fig. SI 11). At 1 % extract, viability was higher than at 100 % and 10 % but still reduced compared to CTRL. Statistical analysis revealed significant differences among the experimental groups (Fig. 5). On day 1, G06 showed significantly lower viability than G00 and G02 ($p < 0.01$). At day 3, G04 displayed significantly higher viability than G00 and G02 ($p < 0.01$), while G06 was also higher than G02 ($p < 0.01$) and G00 ($p < 0.05$). On day 7, no significant differences were observed between the conditions. This behavior was expected; by increasing the time of Fe-based alloys when in contact with the extract cell solution, an increase in degradation products was observed [65].

4. Discussion

FTIR analysis (Fig. SI 2) showed the effect of glycine addition to DES containing Fe and Mn ions. The increase in glycine presented a shift of the bonds to lower wavenumbers, indicating the formation of metal-ligand interactions, weakening the bond strength in the carboxylate group [66]. The electrochemical analysis revealed a significant correlation between glycine concentration and Mn reduction. It was observed that the addition of glycine shifted the potential to negative values (Fig. SI 3), which allows the reduction of Mn^{2+} to metallic Mn^0 [54].

The findings align with Guo et al. [47] research on the effect of glycine in DES electrodeposition and Mn incorporation. The inclusion of Mn, enabled by glycine as a complexing agent, acted as a micro-galvanic site. Mn tends to oxidize, enhancing the negative charges at the metal surface/electrolyte interface and increasing the corrosion current density (j_{corr}) [25,67]. Condition G06, with the highest glycine concentration, exhibited a corrosion rate of 1.3 mm/yr, significantly higher than G00 (0.4 mm/yr) and when compared with sintered Fe-30Mn alloy (0.7 mm/yr) [25]. This trend is consistent with prior studies that attribute increased corrosion rates in Fe-Mn alloys to Mn [13,68]. Statistical analysis of the corrosion rates (one-way ANOVA, $p < 0.05$) revealed that the degradation rate of G06 was significantly higher than that of G00 and consistent with the effect of higher Mn incorporation. Detailed results of the pairwise comparisons are presented in Table SI 7. Electrochemical impedance spectroscopy (EIS) also demonstrated reduced impedance values for glycine-containing conditions, further agreeing with the observed degradation behavior.

Mechanical tests revealed that adding glycine influenced the hardness and structural uniformity of the electroformed conditions. Vickers and Knoop hardness values increased significantly with glycine concentration, indicating enhanced mechanical strength. Similar behavior was observed by Juma et al. [44]. They studied the effect of four different additives (nicotinic acid, methyl nicotinate, dimethyl hydantoin, and boric acid) in the electrodeposition process of pure Co. They observed an increase in the hardness of the deposited Co using those additives (~ 455 – 588 HV) compared with the condition without (~ 382 HV). The layer-by-layer growth observed in the cross-sectional analysis of G04 and G06 further highlights the impact of glycine on nucleation dynamics. While glycine promoted the formation of a harder material, it could also introduce localized weaknesses, such as needle-shaped features, which may compromise mechanical reliability under dynamic loads. The value of condition G00 is within the range reported by Gambaro et al., *who* analysed the mechanical properties of three Fe-Mn alloys for biomedical application (Fe-12Mn-1.2C, Fe-16Mn-0.9C, and Fe-20Mn-0.6C) and observed that increasing the Mn amount, the Vickers hardness decreased from ~ 380 HV to ~ 280 HV. The differences observed among the hardness values were confirmed by statistical analysis (one-way ANOVA, $p < 0.05$), which indicated that condition G06 was significantly harder than G00 and G02. In contrast, no significant difference was found between G00 and G02. Complete

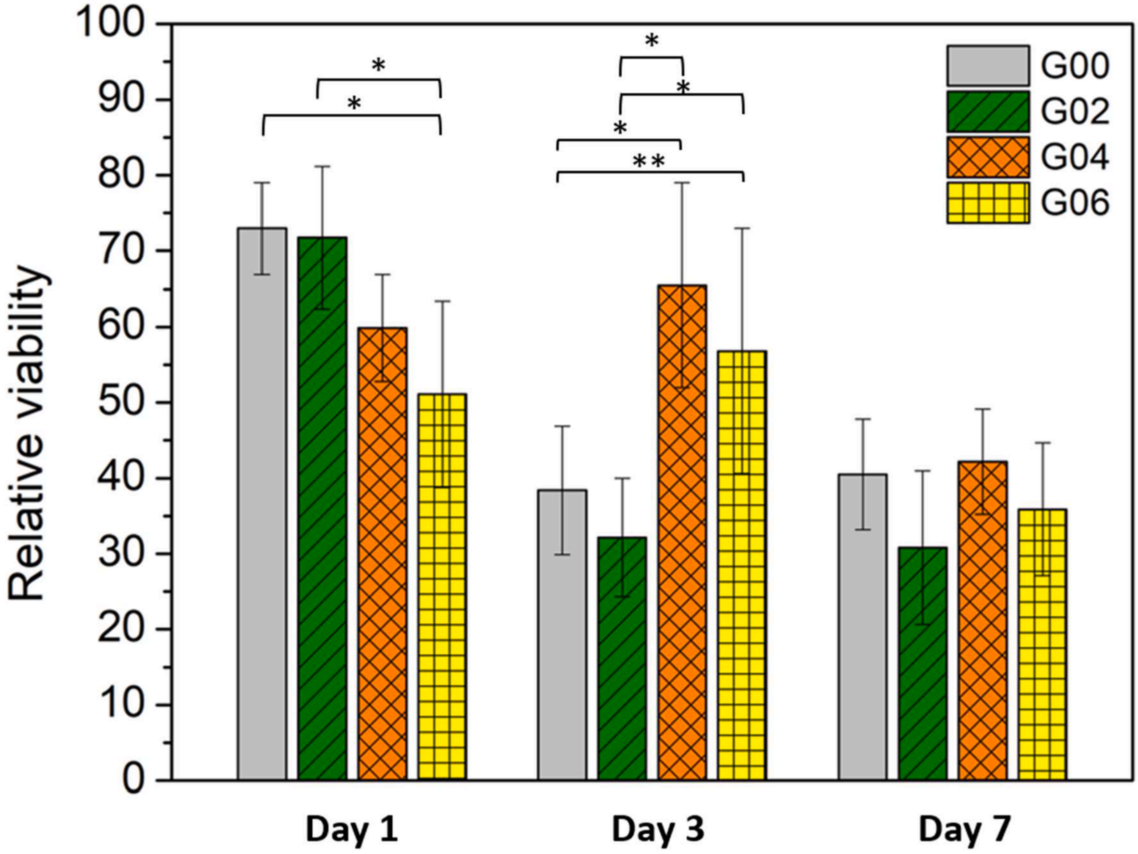

Fig. 5. Alamar Blue Viability of HUVECs after exposure to 1 % extracts of Fe and Fe-Mn alloys (G00, G02, G04, G06) for 1, 3, and 7 days, expressed as percentage of CTRL (mean ± 95 % CI, $n = 6$). Statistical analysis was performed, and $^{**}p < 0.05$, $^{*}p < 0.01$ values were considered. Results for 100 % and 10 % extracts are provided in the Supplementary Information (Fig. S1).

statistical comparisons are provided in Table SI 10.

Surface morphology and crystallinity of the electroformed materials provided additional insights into the observed corrosion and mechanical properties. The chemical etching (Fig. SI 3) revealed a layer-by-layer nucleation behavior in glycine conditions. On a stepwise surface, the atoms attach to kinks at the steps, resulting in the motion of steps along the plane until the whole layer is covered. This mechanism is called a layer-by-layer growth mode [57]. As observed in SEM micrographs, the formation of a needle-shaped feature at higher glycine concentrations likely increased surface area, which could be related to an increase in the corrosion rate [69]. This feature is commonly associated with rapid nucleation during the electrodeposition [70]. The XRD patterns further revealed that conditions G04 and G06 achieved crystalline α-Fe with a bcc structure, contrasting with the amorphous nature of G00 and G02. These structural changes, driven by the metal ions' complexation with glycine, may also contribute to the variability in their mechanical and degradation behavior [45]. The effect of additives on the crystallinity of electrodeposited metals has already been discussed in the literature [44, 71]. Surface roughness showed no statistical difference between the conditions (Fig. SI 7 and Table SI 4).

Although the elemental analysis mainly revealed Fe, Mn, and O (Table SI 3), the electrolyte composition ($CaCl_2$ and H_3BO_3) raises the possibility of surface incorporation of Ca and B species. Previous works have shown that Ca-based eutectic electrolytes can affect nucleation and deposit compactness [72], while boron-containing additives may alter deposition kinetics and surface chemistry [73]. Even if not detected in this work by EDS spectra (Fig. SI 5) and EPMA (Fig. SI 6 and SI 7), the potential presence of these elements at trace levels cannot be excluded. Such incorporation may have relevant implications for both corrosion and biological behavior: Ca species could favor the formation of Ca-phosphate corrosion products, temporarily stabilizing degradation layers and enhancing bioactivity, whereas B species may modify local pH and interfere with passivation, potentially accelerating dissolution under physiological conditions [74]. This dual effect suggests that the electrolyte formulation may subtly modulate the early corrosion kinetics and cellular response.

Biological performance of the alloys was assessed via indirect cytotoxicity tests using HUVECs. Exposure to 100 % extract media caused a marked reduction in cell viability for all conditions, confirming a general concentration-dependent cytotoxic effect. At lower extract concentrations (10 % and 1 %), temporal differences became evident: on day 1, G00 and G02 supported higher viability, while on day 3, the best results were observed for G04 and G06. This transient improvement was likely due to partial passivation, which temporarily reduced ion release and improved cell tolerance. After 7 days, however, viability decreased in all groups and differences among them became negligible, reflecting the cumulative effect of degradation products over time, highlighting the need to control the release of metal ions and degradation by-products to minimize cytotoxic effects [75].

The biological trends correlate with the microstructural and electrochemical results. XRD revealed that higher glycine concentrations promoted ferrite crystallization, which is typically associated with higher corrosion susceptibility. Indeed, G06 showed the highest corrosion rate and a sharper decline in viability upon longer exposure, suggesting that the accelerated release of Fe and Mn ions exceeded cellular tolerance [65]. Mechanical tests also indicated that the same condition exhibited higher hardness, reinforcing the trade-off between strengthening through crystallinity and the biological response imposed by faster degradation. These findings suggest that glycine concentration has an effect: while higher levels improve mechanical properties, they also increase corrosion-driven ion release, reducing cytocompatibility.

5. Conclusions

Electroformed Fe-Mn with 75 – 85 μm thickness were produced using DES based on ethylene glycol and glycine as a complexing agent. Glycine addition improved Mn incorporation, increased current efficiency, and significantly altered the microstructure and corrosion behavior of the electroformed samples. Surface roughness and cytotoxicity analysis did not change significantly among the studied conditions. However, electrochemical tests showed different corrosion behaviors, especially between conditions G00 and G06. The analysis presented a decrease in the corrosion resistance due to the presence of Mn in the alloy. Mn acted as a corrosion site, accelerating the corrosion rate of the electroformed samples.

Further experiments are required to optimize the electroforming process. Applying different additives increases Mn content, decreases roughness to a nm scale, and improves mechanical properties. Needle-shaped nucleation should be avoided to improve the mechanical properties of electroformed metals, allowing the use of this material in biomedical devices. Long-term studies in simulated physiological solutions and in vivo tests will be required to fully establish the degradation kinetics and the tissue response to electroformed Fe-Mn alloys.

CRediT authorship contribution statement

Vinicius Sales: Writing – review & editing, Writing – original draft, Software, Methodology, Investigation, Formal analysis, Data curation, Conceptualization. **Carlo Paternoster:** Writing – review & editing, Validation, Supervision, Project administration, Investigation, Conceptualization. **Francesco Copes:** Writing – review & editing, Writing – original draft, Validation, Formal analysis. **Paolo Mengucci:** Writing – review & editing, Validation, Formal analysis, Data curation. **Gabriele Grima:** Writing – review & editing, Methodology, Investigation, Formal analysis, Data curation. **Marcello Cabibbo:** Writing – review & editing, Formal analysis. **Georgios Kolliopoulos:** Writing – review & editing, Validation, Supervision, Resources, Project administration, Funding acquisition, Conceptualization. **Diego Mantovani:** Writing – review & editing, Visualization, Validation, Supervision, Resources, Project administration, Funding acquisition.

Declaration of competing interest

The authors declare that they have no known competing financial interests or personal relationships that could have appeared to influence the work reported in this paper.

Acknowledgments

This work was mainly supported by NSERC—Canada under the CU-I2I and Alliance programs, and by the Fonds de Recherche du Quebec (Strategia program). D.M. was supported by NSERC—Canada Discovery and holds a Canada Research Chair Tier I. G.K. was supported by NSERC—Canada (Discovery Grant) and FRQNT (ERA-MIN 2). The financial support of the Canada Foundation for Innovation (CFI) is also acknowledged.

Supplementary materials

Supplementary material associated with this article can be found, in the online version, at doi:10.1016/j.bbiosy.2025.100123.

Data availability

Data will be made available on request.

References

[1] Borges MHR, Nagay BE, Costa RC, Souza JGS, Mathew MT, Barão VAR. Recent advances of polypyrrole conducting polymer film for biomedical application: toward a viable platform for cell-microbial interactions. Adv Colloid Interface Sci 2023;314. https://doi.org/10.1016/j.cis.2023.102860.

[2] Aufa AN, Hassan MZ, Ismail Z. Recent advances in Ti-6Al-4V additively manufactured by selective laser melting for biomedical implants: prospect development. J Alloys Compd 2022;896. https://doi.org/10.1016/j.jallcom.2021.163072.

[3] Gautam S, Bhatnagar D, Bansal D, Batra H, Goyal N. Recent advancements in nanomaterials for biomedical implants. Biomed Eng Adv 2022;3:100029. https://doi.org/10.1016/j.bea.2022.100029.

[4] Thanigachalam M, Muthusamy Subramanian AV. Evaluation of PEEK-TiO2- SiO2 nanocomposite as biomedical implants with regard to in-vitro biocompatibility and material characterization. J Biomater Sci Polym Ed 2022;33:727–46. https://doi.org/10.1080/09205063.2021.2014028.

[5] Venkateswarlu B, Sunil BR, Kumar RS. Magnesium based alloys and composites: revolutionized biodegradable temporary implants and strategies to enhance their performance. Materialia (Oxf) 2023:27. https://doi.org/10.1016/j.mtla.2023.101680.

[6] Prasadh S, Raguraman S, Wong R, Gupta M. Current status and outlook of temporary implants (Magnesium/Zinc) in cardiovascular applications. Metals (Basel) 2022:12. https://doi.org/10.3390/met12060999.

[7] Bazhenov V, Koltygin A, Komissarov A, Li A, Bautin V, Khasenova R, Anishchenko A, Seferyan A, Komissarova J, Estrin Y. Gallium-containing magnesium alloy for potential use as temporary implants in osteosynthesis. J Magnes Alloys 2020;8:352–63. https://doi.org/10.1016/j.jma.2020.02.009.

[8] Kumar P, Anne G, Ramesh MR, Doddamani M, Prabhu A. Enhancing the functionality of biodegradable Mg–Zn–Mn alloys using poly(lactic) acid (PLA) coating for temporary implants. J Coat Technol Res 2024;21:1525–37. https://doi.org/10.1007/s11998-024-00913-8.

[9] Wiebe J, Nef HM, Hamm CW. Current status of bioresorbable scaffolds in the treatment of coronary artery disease. J Am Coll Cardiol 2014;64:2541–51. https://doi.org/10.1016/j.jacc.2014.09.041.

[10] Ang HY, Ng J, Bulluck H, Wong P, Venkatraman S, Huang Y, Foin N. Fundamentals of bioresorbable stents. Functionalised Cardiovascular Stents 2018:75–97. https://doi.org/10.1016/b978-0-08-100496-8.00005-6.

[11] Zheng YF, Gu XN, Witte F. Biodegradable metals. Materials Science and Engineering R: Reports 2014;77:1–34. https://doi.org/10.1016/j.mser.2014.01.001.

[12] Li H, Zheng Y, Qin L. Progress of biodegradable metals. Progress Natural Sci: Mater Int 2014;24:414–22. https://doi.org/10.1016/j.pnsc.2014.08.014.

[13] He J, He FL, Li DW, Liu YL, Liu YY, Ye YJ, Yin DC. Advances in Fe-based biodegradable metallic materials. RSC Adv 2016;6:112819–38. https://doi.org/10.1039/C6RA20594A.

[14] Wegener B, Sievers B, Utzschneider S, Müller P, Jansson V, Rößler S, Nies B, Stephani G, Kieback B, Quadbeck P. Microstructure, cytotoxicity and corrosion of powder-metallurgical iron alloys for biodegradable bone replacement materials. Mater Sci Eng B Solid State Mater Adv Technol 2011;176:1789–96. https://doi.org/10.1016/j.mseb.2011.04.017.

[15] Carluccio D, Bermingham M, Kent D, Demir AG, Previtali B, Dargusch MS. Comparative Study of Pure Iron Manufactured by Selective Laser Melting, Laser Metal Deposition, and Casting Processes. Adv Eng Mater 2019;21. https://doi.org/10.1002/adem.201900049.

[16] Xu W, Lu X, Tan L, Yang K. Study on properties of a novel biodegradable Fe-30Mn-1C alloy. Jinshu Xuebao/Acta Metallurgica Sinica 2011;47:1342–7. https://doi.org/10.3724/SP.J.1037.2011.00258.

[17] Peuster M, Hesse C, Schloo T, Fink C, Beerbaum P, von Schnakenburg C. Long-term biocompatibility of a corrodible peripheral iron stent in the porcine descending aorta. Biomaterials 2006;27:4955–62. https://doi.org/10.1016/j.biomaterials.2006.05.029.

[18] Schinhammer M, Hänzi AC, Löffler JF, Uggowitzer PJ. Design strategy for biodegradable Fe-based alloys for medical applications. Acta Biomater 2010;6:1705–13. https://doi.org/10.1016/j.actbio.2009.07.039.

[19] Sharma P, Pandey PM. Corrosion rate modelling of biodegradable porous iron scaffold considering the effect of porosity and pore morphology. Mater Sci Eng C 2019:103. https://doi.org/10.1016/j.msec.2019.109776.

[20] Md Yusop AH, Al Sakkaf A, Nur H. Modifications on porous absorbable Fe-based scaffolds for bone applications: a review from corrosion and biocompatibility viewpoints. J Biomed Mater Res B Appl Biomater 2022;110:18–44. https://doi.org/10.1002/jbm.b.34893.

[21] Rybalchenko OV, Anisimova NY, Kiselevsky MV, Rybalchenko GV, Martynenko NS, Bochvar NR, Tabachkova NY, Shchetinin IV, Shibaeva TV, Konushkin SV, Tokar AA, Raab AG, Dobatkin SV. Effect of equal-channel angular pressing on structure and properties of Fe-Mn-C alloys for biomedical applications. Mater Today Commun 2022;30. https://doi.org/10.1016/j.mtcomm.2021.103048.

[22] Heiden M, Nauman E, Stanciu L. Bioresorbable Fe–Mn and Fe–Mn–HA Materials for Orthopedic Implantation: enhancing Degradation through Porosity Control. Adv Healthc Mater 2017;6. https://doi.org/10.1002/adhm.201700120.

[23] Gebert A, Kochta F, Voß A, Oswald S, Fernandez-Barcia M, Kühn U, Hufenbach J. Corrosion studies on Fe-30Mn-1C alloy in chloride-containing solutions with view to biomedical application. Mater Corrosion 2018;69:167–77. https://doi.org/10.1002/maco.201709476.

[24] Gambaro S, Paternoster C, Occhionero B, Fiocchi J, Biffi CA, Tuissi A, Mantovani D. Mechanical and degradation behavior of three Fe-Mn-C alloys for potential

biomedical applications. Mater Today Commun 2021;27. https://doi.org/10.1016/j.mtcomm.2021.102250.

[25] Hermawan H, Dubé D, Mantovani D. Degradable metallic biomaterials: design and development of Fe-Mn alloys for stents. J Biomed Mater Res A 2010;93:1–11. https://doi.org/10.1002/jbm.a.32224.

[26] Schinhammer M, Gerber I, Hänzi AC, Uggowitzer PJ. On the cytocompatibility of biodegradable Fe-based alloys. Mater Sci Eng C 2013;33:782–9. https://doi.org/10.1016/j.msec.2012.11.002.

[27] Liu P, Yao C, Zhang W, Yang Q, Li G, Tong Y, Hope GA. Electrochemical preparation of Fe – Mn alloy film in organic bath. Thin Solid Films 2008;516: 3935–9. https://doi.org/10.1016/j.tsf.2007.07.203.

[28] Moravej M, Prima F, Fiset M, Mantovani D. Electroformed iron as new biomaterial for degradable stents: development process and structure-properties relationship. Acta Biomater 2010;6:1726–35. https://doi.org/10.1016/j.actbio.2010.01.010.

[29] Parkinson R. Electroforming-a unique metal fabrication process. Toronto: Nickel development institute; 1998.

[30] Hart T, Watson A. Eelectroforming. Metal Finishing 2000;98:388–99. https://doi.org/10.1016/S0026-0576(00)80348-7.

[31] Harty SF, McGeough JA, Tulloch RM. A review of the electroforming of iron and iron-nickel alloy. Surface Technol 1981;12:39–55. https://doi.org/10.1016/0376-4583(81)90135-7.

[32] Shen C, Zhu Z, Zhu D. Surface Self-nanocrystallization in Copper Electroforming. J Mater Eng Perform 2019;28:211–20. https://doi.org/10.1007/s11665-018-3793-9.

[33] Bozzini B, Cavallotti PL, Fanigliulo A, Giovannelli G, Mele C, Natali S. Electrodeposition of white gold alloys: an electrochemical, spectroelectrochemical and structural study of the electrodeposition of Au-Sn alloys in the presence of 4-cyanopyridine. J Solid State Electrochem 2004:147–58. https://doi.org/10.1007/s10008-003-0434-4.

[34] Beltowska-lehman E, Bigos A, Indyka P, Kot M. Surface & Coatings Technology Electrodeposition and characterisation of nanocrystalline Ni – Mo coatings. Surf Coat Technol 2012;211:67–71. https://doi.org/10.1016/j.surfcoat.2011.10.011.

[35] Zhang Q, De Oliveira Vigier K, Royer S, Jérôme F. Deep eutectic solvents: syntheses, properties and applications. Chem Soc Rev 2012;41:7108–46. https://doi.org/10.1039/c2cs35178a.

[36] Smith EL, Abbott AP, Ryder KS. Deep Eutectic Solvents (DESs) and Their Applications. Chem Rev 2014;114:11060–82. https://doi.org/10.1021/cr300162p.

[37] Abbott AP, Alabdullah SSM, Al-Murshedi AYM, Ryder KS. Brønsted acidity in deep eutectic solvents and ionic liquids. Faraday Discuss 2018;206:365–77. https://doi.org/10.1039/c7fd00153c.

[38] Plaza-Mayoral E, Dalby KN, Falsig H, Chorkendorff I, Sebastián-Pascual P, Escudero-Escribano M. Preparation of Tunable Cu−Ag Nanostructures by Electrodeposition in a Deep Eutectic Solvent. ChemElectroChem 2024;11. https://doi.org/10.1002/celc.202400094.

[39] Wang Z, Wu T, Ru J, Hua Y, Bu J, Wang D. Eco-friendly preparation of nanocrystalline Fe-Cr alloy coating by electrodeposition in deep eutectic solvent without any additives for anti-corrosion. Surf Coat Technol 2021;406. https://doi.org/10.1016/j.surfcoat.2020.126636.

[40] Zhou J, Meng X, Ouyang P, Zhang R, Liu H, Xu C, Liu Z. Electrochemical behavior and electrodeposition of Fe-Co-Ni thin films in choline chloride/urea deep eutectic solvent. Journal of Electroanalytical Chemistry 2022;919. https://doi.org/10.1016/j.jelechem.2022.116516.

[41] Chen Q, Wang Q, Lu S. Electrodeposition of Magnesium in Deep Eutectic Solvents Based on Magnesium Chloride Hexahydrate and Choline Chloride with Urea Added. J Phys Conf Ser, Institute of Physics 2024. https://doi.org/10.1088/1742-6596/2731/1/012056.

[42] Wang Z, Wu T, Geng X, Ru J, Hua Y, Bu J, Xue Y, Wang D. The role of electrolyte ratio in electrodeposition of nanoscale Fe–Cr alloy from choline chloride-ethylene glycol ionic liquid: a suitable layer for corrosion resistance. J Mol Liq 2022;346. https://doi.org/10.1016/j.molliq.2021.117059.

[43] Tomé LIN, Baião V, da Silva W, Brett CMA. Deep eutectic solvents for the production and application of new materials. Appl Mater Today 2018;10:30–50. https://doi.org/10.1016/j.apmt.2017.11.005.

[44] Juma JA. The effect of organic additives in electrodeposition of Co from deep eutectic solvents. Arab J Chem 2021;14. https://doi.org/10.1016/j.arabjc.2021.103036.

[45] Alesary HF, Cihangir S, Ballantyne AD, Harris RC, Weston DP, Abbott AP, Ryder KS. Influence of additives on the electrodeposition of zinc from a deep eutectic solvent. Electrochim Acta 2019;304:118–30. https://doi.org/10.1016/j.electacta.2019.02.090.

[46] Ibrahim S, Bakkar A, Ahmed E, Selim A. Effect of additives and current mode on zinc electrodeposition from deep eutectic ionic liquids. Electrochim Acta 2016;191: 724–32. https://doi.org/10.1016/j.electacta.2016.01.110.

[47] Guo J, Guo X, Wang S, Zhang Z, Dong J, Peng L, Ding W. Effects of glycine and current density on the mechanism of electrodeposition, composition and properties of Ni-Mn films prepared in ionic liquid. Appl Surf Sci 2016;365:31–7. https://doi.org/10.1016/j.apsusc.2015.12.248.

[48] Su CW, Yang W, Guo JM, Zhang YJ. Modulated morphology of Fe foils electrodeposited at a high current density by adding cations. Vacuum 2012;86: 2095–101. https://doi.org/10.1016/j.vacuum.2012.05.032.

[49] Sides WD, Huang Q. Electrodeposition of manganese thin films on a rotating disk electrode from choline chloride/urea based ionic liquids. Electrochim Acta 2018; 266:185–92. https://doi.org/10.1016/j.electacta.2018.01.120.

[50] Practice for Calculation of Corrosion Rates and Related Information from Electrochemical Measurements, (2023). https://doi.org/10.1520/G0102-23.

[51] Böck R, Wulf SE. Electrodeposition of iron films from an ionic liquid (ChCl/urea/FeCl 3 deep eutectic mixtures). Trans Instit Metal Finish 2009;87:28–32. https://doi.org/10.1179/174591908X379601.

[52] Panzeri G, Accogli A, Gibertini E, Rinaldi C, Nobili L, Magagnin L. Electrodeposition of high-purity nanostructured iron films from Fe(II) and Fe(III) non-aqueous solutions based on ethylene glycol. Electrochim Acta 2018;271: 576–81. https://doi.org/10.1016/j.electacta.2018.03.174.

[53] Deng MJ, Chen PY, Sun IW. Electrochemical study and electrodeposition of manganese in the hydrophobic butylmethylpyrrolidinium bis((trifluoromethyl) sulfonyl)imide room-temperature ionic liquid. Electrochim Acta 2007;53:1931–8. https://doi.org/10.1016/j.electacta.2007.08.047.

[54] Chang JK, Huang CH, Tsai WT, Deng MJ, Sun IW, Chen PY. Manganese films electrodeposited at different potentials and temperatures in ionic liquid and their application as electrode materials for supercapacitors. Electrochim Acta 2008;53: 4447–53. https://doi.org/10.1016/j.electacta.2008.01.036.

[55] Figueira G, Della Rovere CA, Gargarella P. Electrodeposition of Fe–Mn alloys from chloride-based bath: a preliminary study for biomedical applications. J Mater Res Technol 2021;13:2527–35. https://doi.org/10.1016/j.jmrt.2021.05.103.

[56] Rao S, Zou X, Wang S, Lu Y, Shi T, Hsu HY, Xu Q, Lu X. Electrodeposition of Ni-Cu alloy films from nickel matte in deep eutectic solvent. Mater Chem Phys 2019;232: 6–15. https://doi.org/10.1016/j.matchemphys.2019.04.052.

[57] H.-C. Jeong, E.D. Williams, Steps on surfaces: experiment and theory, 1999.

[58] Harrington DA, Van Den Driessche P. Mechanism and equivalent circuits in electrochemical impedance spectroscopy. Electrochim Acta 2011:8005–13. https://doi.org/10.1016/j.electacta.2011.01.067.

[59] Scully JR. Polarization resistance method for determination of instantaneous corrosion rates. Corrosion 2000;56:199–217. https://doi.org/10.5006/1.3280536.

[60] Fashu S, Khan R. Studies on electrochemical deposition of novel Zn–Mn–Ni ternary alloys from an ionic liquid based on choline chloride. Protection of Metals and Physical Chemistry of Surfaces 2017;53:118–26. https://doi.org/10.1134/S2070205117010051.

[61] Wen C, Zhan X, Huang X, Xu F, Luo L, Xia C. Characterization and corrosion properties of hydroxyapatite/graphene oxide bio-composite coating on magnesium alloy by one-step micro-arc oxidation method. Surf Coat Technol 2017;317: 125–33. https://doi.org/10.1016/j.surfcoat.2017.03.034.

[62] de Freitas Cunha Lins V, de Andrade Reis GF, de Araujo CR, Matencio T. Electrochemical impedance spectroscopy and linear polarization applied to evaluation of porosity of phosphate conversion coatings on electrogalvanized steels. Appl Surf Sci 2006;253:2875–84. https://doi.org/10.1016/j.apsusc.2006.06.030.

[63] De Robertis E, Neves RS, Abrantes LM, Motheo AJ. Pd-P electroless deposition on carbon steel: an electrochemical impedance spectroscopy study. Journal of Electroanalytical Chemistry 2005;581:86–92. https://doi.org/10.1016/j.jelechem.2005.01.040.

[64] Jüttner K. Electrochemical impedance of corrosion processes on surfaces spectroscopy (EIS) inhomogeneous. Electrochemica Acta 1990;35:1501–8.

[65] Loffredo S, Gambaro S, Copes F, Paternoster C, Giguère N, Vedani M, Mantovani D. Effect of silver in thermal treatments of Fe-Mn-C degradable metals: implications for stent processing. Bioact Mater 2022;12:30–41. https://doi.org/10.1016/j.bioactmat.2021.10.020.

[66] Zabihzadeh S, Ionescu C, Biselli S, Blanchard A, Sereda O. Importance of the drying method in crystalline phase formation and metallic elements distribution of glycine complexes. Results Chem 2024;7. https://doi.org/10.1016/j.rechem.2024.101457.

[67] Schinhammer M, Steiger P, Moszner F, Löffler JF, Uggowitzer PJ. Degradation performance of biodegradable FeMnC(Pd) alloys. Materials Science and Engineering C 2013;33:1882–93. https://doi.org/10.1016/j.msec.2012.10.013.

[68] Fajardo S, Llorente I, Jiménez JA, Bastidas JM, Bastidas DM. Effect of Mn additions on the corrosion behaviour of TWIP Fe-Mn-Al-Si austenitic steel in chloride solution. Corros Sci 2019;154:246–53. https://doi.org/10.1016/j.corsci.2019.04.026.

[69] You YH, Gu CD, Wang XL, Tu JP. Electrodeposition of Ni-Co alloys from a deep eutectic solvent. Surf Coat Technol 2012;206:3632–8. https://doi.org/10.1016/j.surfcoat.2012.03.001.

[70] Yuliy GZ, Gamburg D. Theory and practice of metal electrodeposition. New York: Springer; 2011. https://doi.org/10.1007/978-1-4419-9669-5_1.

[71] Chien CW, Liu CL, Chen FJ, Lin KH, Lin CS. Microstructure and properties of carbon-sulfur-containing chromium deposits electroplated in trivalent chromium baths with thiosalicylic acid. Electrochim Acta 2012;72:74–80. https://doi.org/10.1016/j.electacta.2012.03.168.

[72] M.Hartley J, Alle J, Meierl J, Schmidt A, Krossing I, Abbott AP. Calcium chloride-based systems for metal electrodeposition. Electrochim Acta 2022;402. https://doi.org/10.1016/j.electacta.2021.139560.

[73] Forero-Saboya J, Bodin C, Ponrouch A. A boron-based electrolyte additive for calcium electrodeposition. Electrochem Commun 2021;124.

[74] Rabeea MA, Keal ME, Elgar CE, Yang JM, Abbott AP, Hartley JM. Electrodeposition of iron and neodymium...chloride hexahydrate eutectic solvents. Electrochim Acta 2025;533. https://doi.org/10.1016/j.electacta.2025.146517.

[75] Liu B, Zheng YF, Ruan L. In vitro investigation of Fe30Mn6Si shape memory alloy as potential biodegradable metallic material. Mater Lett 2011;65:540–3. https://doi.org/10.1016/j.matlet.2010.10.068.